# Probing Resolved Structures in Luminous Infrared Galaxies

William Meynardie, Aaron Evans, Sean Linden

August 31, 2021

**Abstract**

We studied 47 resolved regions across 23 LIRGs, analyzing the correlation between their radio and infrared emission. We determined the $q_{IR}$-value of each of these regions, and fitted the luminosities to a power-law fitting the form $L_{IR} \propto L_{1.49GHz}^{\gamma}$. We used the resolution of Herschel and Spitzer to separate regions containing AGN from starburst regions. We measured a median $q_{IR}$ of 2.528(55) and a $\gamma$ of 0.873(59) in the starburst regions. Finally, we calculated the star formation rate in each of these regions and found that the infrared, in general, traced less star formation than the radio, highlighting the need to include unobscured ultraviolet data in our comparison.

## 1 Introduction

Luminous Infrared Galaxies (LIRGs) are galaxies which are especially bright at infrared wavelengths, often as a result of a galaxy merger. These objects host some of the most extreme star-forming regions in the local universe, and as a result, they allow us to study star formation in extreme environments.

There is a well-studied correlation between the infrared and radio luminosities of these objects, but previously, this correlation has only been studied on the scale of entire galaxies (Helou et al. 1985, Condon 1992). With data from the Herschel and Spitzer infrared telescopes, we can finally begin to probe these objects at smaller scales. With these data, we can see whether the IR-radio correlation holds for sub-structures within LIRGs, or if it begins to fall apart (Murphy et al. 2006). Additionally, we can use this data to calculate the star formation rate (SFR) in these galaxies. While we don't have the full picture without ultraviolet data from GALEX, we can begin to compare SFR measured with infrared data against SFR measured with radio data. Finally, we can use the results from this work as a calibration as we extend the IR-radio comparisions to higher frequencies.

## 2 Sample Selection

Our sample consists of 47 regions in 23 galaxies, selected based on the presence of extended emission in the Herschel 70 $\mu$m image (Chu et al. 2017).

The criteria for extended emission was as follows: any galaxy with at least one structure that is not a point source; or any galaxy with more than one structure, even if they are all point sources. With these criteria, we identified 91 galaxies with extended emission.

We then cross-referenced these 91 galaxies with those having archival 1.49 GHz data from the VLA (Condon et al. 1990). This narrowed our sample down to 35 galaxies. We then checked the beam sizes for the images of these galaxies, and eliminated the galaxies which had no images with a beam size equal to or smaller than 6.0 arcseconds, because 6.0 arcseconds was our target resolution. This left us with 30 galaxies. Finally, there were 7 galaxies which had a problem with either the 24 $\mu$m, 70 $\mu$m, 100 $\mu$m, or 1.49 GHz image. The most common of these problems was 1.49 GHz images with insufficient cleaning. We eliminated those from the sample, and were left with 23 galaxies.

# 3 Convolution Kernels

Our next step was to convolve the images to our desired resolution of 6.0 arcseconds. This is a process by which the point spread function of the native image is modified to a Gaussian point spread function. For the Herschel and Spitzer images, we used the convolution kernels provided by Aniano et al. (2011).

For the 1.49 GHz images, we convolved each image to a 6.0 arcsecond Gaussian using a Python script. Figure 1 shows an example of the convolution kernels applied to the 1.49 GHz image and 70 $\mu$m image of IRAS F11257+5850, one of the galaxies in our sample.

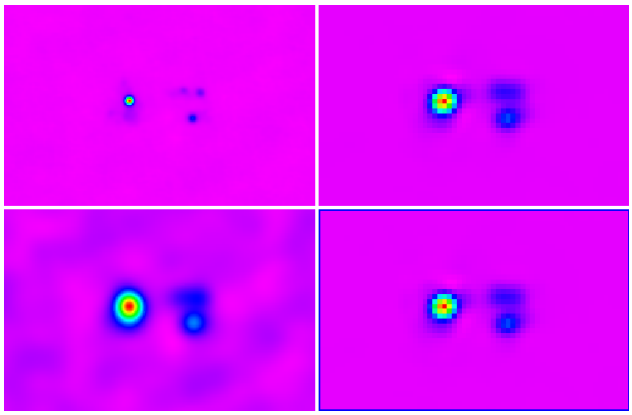

Figure 1: Top-left: native 1.49 GHz image; top-right: native 70 $\mu$m image; bottom-left: convolved 1.49 GHz image; bottom-right: convolved 70 $\mu$m image.

# 4 Aperture Selection

We next selected the size and position of our apertures. We used circular apertures because they are easily repeatable, given the coordinates and radii of the apertures.

There were few objective criteria for the selection of our regions. If two structures in the image were clearly separated, they were always separated into distinct regions. If the emission from a structure was mostly continuous, it was generally kept as one region. Unfortunately, most galaxies fall into an intermediate case, which is much more difficult to determine. If a structure appears to have a tidal tail that is distinct from the nucleus, we attempted to separate them into distinct regions. However, most of this was difficult to determine, and it is mostly subjective.

Additionally, the use of circular apertures is imperfect. Due to the geometry of the apertures, it is often impossible to place the apertures in a way such that they capture all of the emission without overlapping. We prioritized avoiding overlapping apertures over capturing all of the emission.

The greatest advantage to using circular

apertures is that they are easy to repeat, as long as the right ascension, declination, and radius of each aperture is given. The apertures we used are listed in Table 1 below.

| Galaxy | Region | Right Ascension | Declination | Radius ["] |
|---|---|---|---|---|
| F00073+2538 | 1 | 0h 09m 53.2673s | $+25^o$ 55′ 25.849″ | 12 |
| | 2 | 0h 09m 53.7861s | $+25^o$ 55′ 07.442″ | 6.5 |
| | 3 | 0h 09m 52.8252s | $+25^o$ 55′ 43.737″ | 6.5 |
| F00163-1039 | 1 | 0h 18m 50.9082s | $-10^o$ 22′ 37.570″ | 12 |
| | 2 | 0h 18m 50.1522s | $-10^o$ 21′ 40.128″ | 16.5 |
| | 3 | 0h 18m 50.0129s | $-10^o$ 22′ 06.489″ | 10 |
| F00402-2349 | 1 | 0h 42m 45.8067s | $-23^o$ 33′ 41.817″ | 12 |
| | 2 | 0h 42m 52.8210s | $-23^o$ 32′ 28.448″ | 8 |
| F01053-1746 | 1 | 1h 07m 47.3422s | $-17^o$ 30′ 25.284″ | 20 |
| F02114+0456 | 1 | 2h 14m 05.3635s | $+5^o$ 10′ 25.663″ | 20 |
| F02512+1446 | 1 | 2h 54m 01.6245s | $+14^o$ 58′ 13.153″ | 10 |
| F04191-1855 | 1 | 4h 21m 19.9527s | $-18^o$ 48″ 38.532″ | 10 |
| | 2 | 4h 21m 20.0285s | $-18^o$ 48′ 58.422″ | 10 |
| F09437+0317 | 1 | 9h 46m 21.3453s | $+3^o$ 04′ 13.747″ | 35 |
| | 2 | 9h 46m 20.3494s | $+3^o$ 02′ 43.389″ | 25 |
| F10015-0614 | 1 | 10h 04m 01.9448s | $-6^o$ 28′ 25.136″ | 16.5 |
| | 2 | 10h 04m 02.6157s | $-6^o$ 28′ 49.781″ | 10 |
| | 3 | 10h 03m 57.0523s | $-6^o$ 29′ 46.568″ | 15 |
| F11186-0242 | 1 | 11h 21m 12.2182s | $-2^o$ 59′ 3.313″ | 12 |
| F11231+1456 | 1 | 11h 25m 44.9738s | $+14^o$ 40′ 35.478″ | 15 |
| | 2 | 11h 25m 49.4565s | $+14^o$ 40′ 06.449″ | 15 |
| F11257+5850 | 1 | 11h 28m 33.6214s | $+58^o$ 33′ 45.914″ | 10 |
| | 2 | 11h 28m 31.0336s | $+58^o$ 33′ 51.653″ | 7 |
| | 3 | 11h 28m 30.9030s | $+58^o$ 33′ 38.690″ | 6 |
| F13362+4831 | 1 | 13h 38m 17.1403s | $+48^o$ 16′ 60.464″ | 8 |
| | 2 | 13h 38m 17.9436s | $+48^o$ 16′ 42.079″ | 6 |
| F15276+1309 | 1 | 15h 30m 00.7914s | $+12^o$ 59′ 21.983″ | 16 |
| F15437+0234 | 1 | 15h 46m 16.4025s | $+2^o$ 26′ 15.485″ | 20 |
| F16030+2040 | 1 | 16h 05m 13.0753s | $+20^o$ 32′ 28.312″ | 20 |
| F16284+0411 | 1 | 16h 30m 56.5615s | $+4^o$ 04′ 57.881″ | 16 |
| | 2 | 16h 30m 53.2613s | $4^o$ 04′ 22.839″ | 8 |
| F16577+5900 | 1 | 16h 58m 31.6449s | $+58^o$ 56′ 12.674″ | 25 |
| | 2 | 16h 58m 24.0060s | $+58^o$ 57′ 21.765″ | 10 |
| F23007+0836 | 1 | 23h 03m 15.5858s | $+8^o$ 52′ 25.191″ | 18 |
| | 2 | 23h 03m 17.7591s″ | $+8^o$ 53′ 38.722″ | 20 |
| F23157+0618 | 1 | 23h 18m 16.2831s | $+6^o$ 35′ 07.119″ | 25 |
| F23157-0441 | 1 | 23h 18m 22.8439s | $-4^o$ 24′ 56.781″ | 10 |
| | 2 | 23h 18m 21.6421s | $-4^o$ 24′ 55.859″ | 8 |
| | 3 | 23h 18m 22.0890s | $-4^o$ 25′ 08.303″ | 6 |

| | | | | |
|---|---|---|---|---|
| F23254+0830 | 1 | 23h 27m 56.6832s | $+8^o$ 46′ 43.176″ | 14 |
| | 2 | 23h 27m 55.9148s | $+8^o$ 46′ 59.519″ | 6 |
| | 3 | 23h 27m 57.2355s | $+8^o$ 46′ 24.676″ | 6 |
| | 4 | 23h 27m 58.7874s | $+8^o$ 46′ 57.113″ | 10 |
| F23488+1949 | 1 | 23h 51m 24.7689s | $+20^o$ 06′ 40.247″ | 16.5 |
| | 2 | 23h 51m 26.7346s | $+20^o$ 06′ 51.081″ | 13 |
| | 3 | 23h 51m 22.7015s | $+20^o$ 06′ 34.071″ | 13 |
| | 4 | 23h 51m 22.4401s | $+20^o$ 05′ 46.764″ | 15 |

Table 1: Right ascension, declination, and radius of each of the 47 resolved regions in our sample of 23 galaxies..

# 5 Results

We measured the flux density in each of the apertures and calculated the luminosity. The luminosity for the 24 $\mu$m, 70 $\mu$m, and 100 $\mu$m images are presented in units of solar luminosities, $L_\odot$, while the 1.49 GHz luminosity is presented in units of W/Hz. The IR luminosity is calculated using Equation 1 below, and it is presented in units of solar lumionsities, $L_\odot$ (D. Dale, private communication).

$$L_{IR} = 2.176L_{24} - 0.163L_{70} + 1.739L_{100} \quad (1)$$

Our results are given in Table 2 below.

| Galaxy | Region | $\log(L_{1.49\mathrm{GHz}})$ | $\log(L_{24})$ | $\log(L_{70})$ | $\log(L_{100})$ | $\log(L_{IR})$ |
|---|---|---|---|---|---|---|
| F00073+2538 | 1 | 22.4972(62) | 10.086(18) | 10.714(22) | 10.660(32) | 10.989(27) |
| | 2 | 21.01(10) | 8.901(26) | 9.579(32) | 9.604(48) | 9.908(41) |
| | 3 | 21.105(82) | 8.532(38) | 9.303(42) | 9.396(58) | 9.676(53) |
| F00163-1039 | 1 | 22.8214(83) | 10.720(18) | 11.120(23) | 11.009(33) | 11.432(23) |
| | 2 | 21.61(18) | 9.695(24) | 10.307(30) | 10.335(41) | 10.654(35) |
| | 3 | 21.04(41) | 8.793(73) | 9.414(87) | 9.571(90) | 9.870(80) |
| F00402-2349 | 1 | 22.957(11) | 10.497(18) | 11.181(23) | 11.161(33) | 11.470(28) |
| | 2 | 22.778(11) | 10.133(18) | 10.447(28) | 10.403(40) | 11.838(27) |
| F01053-1746 | 1 | 23.4209(54) | 10.914(18) | 11.431(22) | 11.328(32) | 11.703(25) |
| F02114+0456 | 1 | 23.101(11) | 10.531(18) | 11.154(23) | 11.116(33) | 11.444(28) |
| F02512+1446 | 1 | 23.111(21) | 10.950(18) | 11.392(22) | 11.291(32) | 11.694(23) |
| F04191-1855 | 1 | 22.861(27) | 10.238(19) | 11.084(23) | 11.045(34) | 11.324(31) |
| | 2 | 22.847(28) | 10.076(19) | 10.834(25) | 10.804(36) | 11.099(32) |
| F09437+0317 | 1 | 22.795(21) | 9.885(19) | 10.642(24) | 10.792(33) | 11.069(31) |
| | 2 | 22.626(22) | 9.924(19) | 10.673(24) | 10.727(33) | 11.014(30) |
| F10015-0614 | 1 | 22.9229(52) | 10.293(18) | 11.021(23) | 11.038(32) | 11.333(29) |
| | 2 | 22.346(12) | 9.624(20) | 10.223(31) | 10.228(38) | 10.554(31) |
| | 3 | 21.764(68) | 9.338(22) | 10.148(33) | 10.125(39) | 10.409(36) |
| F11186-0242 | 1 | 22.8627(87) | 10.511(18) | 11.046(24) | 11.034(34) | 11.381(27) |
| F11231+1456 | 1 | 23.020(48) | 10.458(19) | 11.273(23) | 11.243(33) | 11.526(31) |
| | 2 | 22.763(87) | 10.203(20) | 10.961(25) | 10.938(36) | 11.232(32) |

| | | | | | | |
|---|---|---|---|---|---|---|
| F11257+5850 | 1 | 23.0378(25) | 10.781(17) | 11.439(22) | 11.211(31) | 11.567(25) |
| | 2 | 22.3049(93) | 10.448(18) | 10.770(22) | 10.609(32) | 11.087(21) |
| | 3 | 22.3206(77) | 10.628(18) | 10.786(22) | 10.566(32) | 11.166(18) |
| F13362+4831 | 1 | 23.209(11) | 10.540(18) | 11.146(23) | 11.074(33) | 11.413(27) |
| | 2 | 22.964(14) | 10.193(18) | 10.552(27) | 10.435(40) | 10.878(27) |
| F15276+1309 | 1 | 22.4419(89) | 10.137(18) | 10.710(23) | 10.711(32) | 11.045(27) |
| F15437+0234 | 1 | 22.5081(88) | 10.221(18) | 10.780(22) | 10.772(32) | 11.111(26) |
| F16030+2040 | 1 | 22.7969(56) | 10.137(18) | 10.754(23) | 10.716(32) | 11.046(27) |
| F16284+0411 | 1 | 22.792(13) | 10.510(18) | 11.157(23) | 11.131(33) | 11.450(28) |
| | 2 | 21.27(21) | 9.257(32) | 9.656(56) | 9.525(95) | 9.956(63) |
| F16577+5900 | 1 | 23.2543(33) | 10.006(18) | 11.027(22) | 11.128(32) | 11.377(31) |
| | 2 | 22.056(21) | 9.614(19) | 10.281(25) | 10.274(35) | 10.586(30) |
| F23007+0836 | 1 | 23.1300(25) | 10.952(17) | 11.266(22) | 11.171(31) | 11.626(21) |
| | 2 | 22.310(18) | 9.534(19) | 10.238(24) | 10.300(34) | 10.594(30) |
| F23157+0618 | 1 | 22.602(12) | 10.073(18) | 10.775(22) | 10.781(32) | 11.083(28) |
| F23157-0441 | 1 | 22.676(26) | 10.132(18) | 10.902(23) | 10.821(33) | 11.120(29) |
| | 2 | 22.863(13) | 10.307(18) | 10.680(24) | 10.582(35) | 11.012(24) |
| | 3 | 22.158(51) | 9.100(29) | 9.689(45) | 9.724(59) | 10.047(50) |
| F23254+0830 | 1 | 23.7444(16) | 10.944(18) | 11.006(24) | 10.947(34) | 11.516(19) |
| | 2 | 21.17(25) | 8.762(51) | 9.16(15) | 9.35(14) | 9.69(11) |
| | 3 | 21.19(24) | 8.733(53) | 9.17(15) | 9.33(15) | 9.66(12) |
| | 4 | 22.068(54) | 9.442(24) | 10.142(35) | 10.139(49) | 10.443(43) |
| F23488+1949 | 1 | 22.7373(36) | 10.130(18) | 11.002(23) | 11.034(32) | 11.303(30) |
| | 2 | 21.943(18) | 9.347(19) | 10.098(31) | 10.192(41) | 10.476(37) |
| | 3 | 21.930(18) | 9.110(20) | 9.901(36) | 10.011(46) | 10.286(42) |
| | 4 | 22.103(14) | 9.739(18) | 10.191(29) | 10.126(42) | 10.514(31) |

Table 2: Photometric data for each of the 47 resolved regions in our sample. $L_{1.49GHz}$ is given in units of W/Hz, and $L_{24}$, $L_{70}$, $L_{100}$, and $L_{IR}$ are given in units of $L_{\odot}$.

## 5.1 Q Results

Next, we calculated $q$-values for each of the galaxies. This value is defined as the log of the ratio of two luminosities at different frequencies, shown by Equation 2 below, where $L_1$ and $L_2$ are the luminosities at frequencies $\nu_1$ and $\nu_2$ respectively.

$$q = \log_{10}\left(\frac{L_1/\nu_1}{L_2/\nu_2}\right) \tag{2}$$

We calculated $q_{IR}$ for each of the galaxies, where $L_1$ and $L_2$ are $L_{IR}$ and $L_{1.49GHz}$ respectively, and $\nu_1$ and $\nu_2$ are 1.49 GHz and 3.75 THz respectively.

We plotted $q_{IR}$ against the 1.49 GHz luminosity, and this plot is given in Figure 2 below. The data points are color-coded based on their optical classification: green represents an H II region, red represents a LINER, yellow represents a Seyfert 1, orange represents a Seyfert 2, and blue represents an unclassified region. Additionally, any data points represented with triangles show the presence of a [Ne V] line, an indicator of an

AGN. (Additional q plots are given in Figures 8-10 in the appendix.)

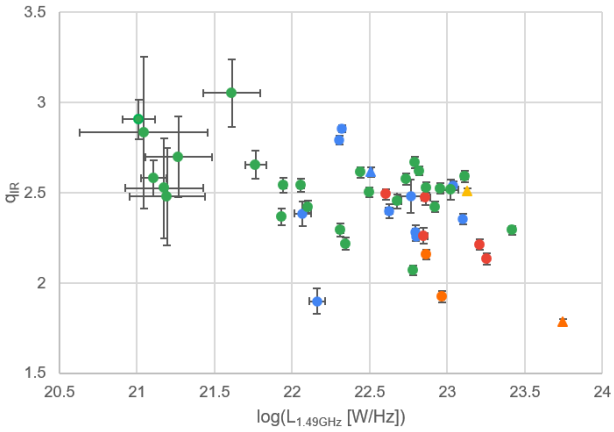


Figure 2: Plot of $q_{IR}$ for resolved regions.

For comparison's sake, the median $q_{IR}$ of normal galaxies is 2.64(2) (Bell 2003). The median $q_{IR}$ of our sample is 2.492(47). There is a noticeable downward trend, so it is already clear that the correlation is non-linear. We believed AGN contamination was likely driving our results downward, so we removed the regions which appear to be contaminated by AGN, and this plot is shown in Figure 3 below.

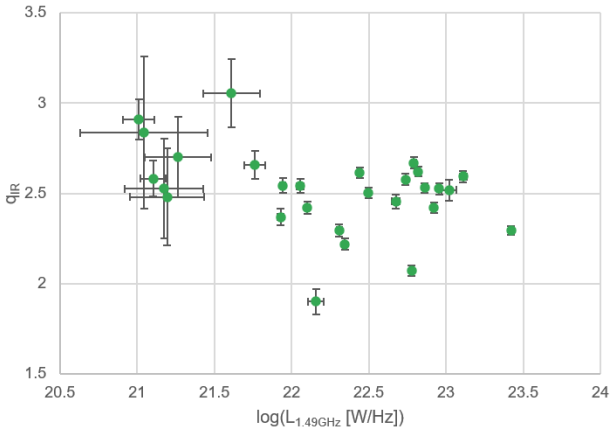


Figure 3: Plot of $q_{IR}$ for resolved H II regions.

Removing the AGN contaminated regions from our results yielded a median $q_{IR}$ of 2.528(55). As we expected, our median $q_{IR}$ went up when we removed AGN contaminated regions. This is within $3\sigma$ of the expected value of 2.64 from the literature. We also find that the downward trend is less steep, indicating that the relationship between $L_{IR}$ and $L_{1.49GHz}$ is closer to linear.

## 5.2 $\gamma$ Results

We next fitted the relationship between the infrared luminosities and the 1.49 GHz luminosity to a power law by plotting them on a log-log plot. The fit we are applying has the form of Equation 3 below, where the slope of the best-fit line is $\gamma$.

$$L_{IR} \propto L_{1.49\text{GHz}}^{\gamma} \tag{3}$$

For comparison, Matthews et al. (2021) found a sublinear correlation ($\gamma = 0.85$) when $\log(L_{1.49GHz}[\text{W/Hz}]) < 22.5$, and a roughly linear correlation ($\gamma = 1$) when $\log(L_{1.49GHz}[\text{W/Hz}]) \geq 22.5$. Our sample ranges from about $21.0 < \log(L_{1.49GHz}[\text{W/Hz}]) < 23.5$. Because we are fitting a single line across all of our data, the results from Matthews et al. indicate that we should find $\gamma$ to be between 0.85 and 1.

Our $\gamma$ plot is shown in Figure 4 below. (Additional $\gamma$ plots are given in Figures 11-13 in the appendix.)

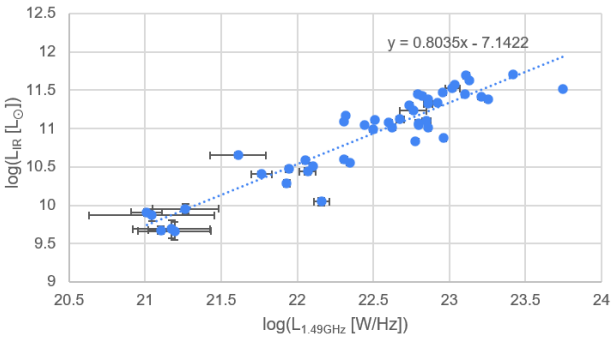


Figure 4: $\gamma = 0.803(48)$ for the full sample.

We then removed the data points with possible AGN contamination and plotted just the H II regions. This plot is shown in Figure 5 below.

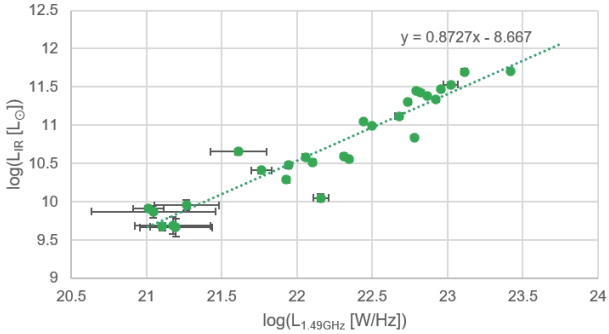


Figure 5: $\gamma = 0.873(59)$ for the H II regions.

Removing the AGN contaminated regions increases the slope, which indicates AGN contamination is making our slope more shallow. Our result of $\gamma = 0.873(59)$ is consistent with the results found by Matthews et al.

## 5.3 SFR Results

Finally, we calculated the SFR using equations given in Murphy et al. (2012). We plotted the SFR calculated from the infrared data against the SFR calculated from the 1.49 GHz data, and this plot is shown in Figure 6 below.

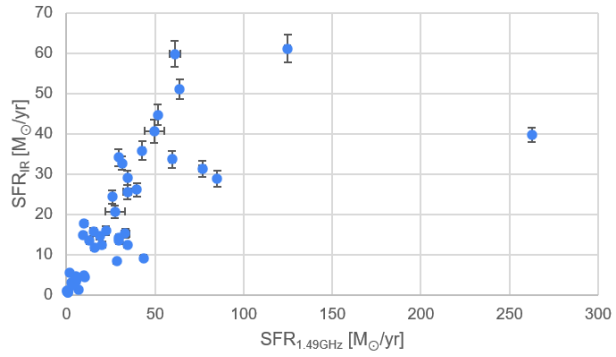


Figure 6: $\mathrm{SFR}_{IR}$ as a function of $\mathrm{SFR}_{1.49GHz}$ for resolved structures in our sample.

There are quite a few outliers in this plot, so we again removed the data points with possible AGN contamination. This plot is shown in Figure 7 below.

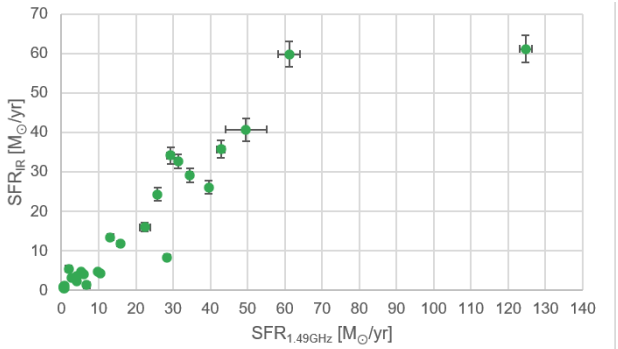


Figure 7: $\mathrm{SFR}_{IR}$ as a function of $\mathrm{SFR}_{1.49GHz}$ for H II regions in our sample.

This removes most of the outliers, but there is still a data point with $\mathrm{SFR}_{1.49GHz}$ between 120 and 130 $M_\odot$/yr that is clearly an outlier. This data point corresponds to IRAS 01053-1746, or VV 114. Although this galaxy is classified as an H II region, there is some speculation that VV 114 is a "Taffy Galaxy," a galaxy in which there is excess radio emission due to shocks from the interaction of the two nuclei (Murphy 2013). This would explain the large discrepancy between its radio emission and its infrared emission.

We see that, for the most part, $\mathrm{SFR}_{IR}$ is slightly less than $\mathrm{SFR}_{1.49GHz}$ in most regions. This is consistent with expectations, because while infrared data only traces obscured star formation, radio data traces the total star formation. To make a more meaningful comparison, we will have to include unobscured star formation, which is traced by ultraviolet data, into our comparison. Unobscured star formation accounts for anywhere from 0.1-15% of the total star formation in these galaxies, with a median of 2.5%, so it is imperative that we include these measurements in our comparison (Howell et al. 2010).

# 6 Conclusions

It is clear from all of our results that AGN contamination is greatly overestimating our $L_{1.49GHz}$ measurements in many regions. This highlights the need for high resolution images, so we can separate regions containing AGN from starburst regions.

We found a median $q_{IR}$ of 2.528(55) in our H II regions, about $2.04\sigma$ away from the value for normal galaxies of 2.64.

We found $\gamma_{IR}$ to be 0.873(59) in our H II regions, consistent with the expectation from Matthews et al. that we should find a $\gamma$ between 0.85 and 1.

Finally, we found that infrared data traces less star formation than radio data, highlighting the need to incorporate ultraviolet data into our results.

# 7 Future Works

The next step for this work is to calculate the star formation traced by the ultraviolet, and add it to the star formation traced by the infrared. Because the infrared traces obscured star formation, while the ultraviolet traces unobscured star formation, we can use both to trace the entirety of the star formation. We can then compare this to the star formation traced by the radio. A discrepancy between these would alert us to the likely presence of an AGN, because an AGN would cause us to greatly overestimate the star formation rate using the radio.

Additionally, the infrared data can allow us to calculate the dust mass and dust temperature in these galaxies. For systems with molecular gas data at comparable resolutions, we will be able to calculate their gas-to-dust ratios.

Finally, we can use our results as a calibration as we push the IR-radio correlation to higher radio frequencies.

# References


[Helou et al.(1985)] Helou, G., Soifer, B. T., Rowan-Robinson, M. 1985. Thermal infrared and nonthermal radio : remarkable correlation in disks of galaxies.. The Astrophysical Journal 298, L7–L11. doi:10.1086/184556

[Condon(1992)] Condon, J. J. 1992. Radio emission from normal galaxies.. Annual Review of Astronomy and Astrophysics 30, 575–611. doi:10.1146/annurev.aa.30.090192.003043

[Murphy et al.(2006)] Murphy, E. J. and 27 colleagues 2006. An Initial Look at the Far-Infrared-Radio Correlation within Nearby Star-forming Galaxies Using the Spitzer Space Telescope. The Astrophysical Journal 638, 157–175. doi:10.1086/498636

[Chu et al.(2017)] Chu, J. K. and 26 colleagues 2017. The Great Observatories All-Sky LIRG Survey: Herschel Image Atlas and Aperture Photometry. The Astrophysical Journal Supplement Series 229. doi:10.3847/1538-4365/aa5d15

[Condon et al.(1990)] Condon, J. J., Helou, G., Sanders, D. B., Soifer, B. T. 1990. A 1.49 GHz Atlas of the IRAS Bright Galaxy Sample. The Astrophysical Journal Supplement Series 73, 359. doi:10.1086/191472

[Aniano et al.(2011)] Aniano, G., Draine, B. T., Gordon, K. D., Sandstrom, K. 2011. Common-Resolution Convolution Kernels for Space- and Ground-Based Telescopes. Publications of the Astronomical Society of the Pacific 123, 1218. doi:10.1086/662219

[Bell(2003)] Bell, E. F. 2003. Estimating Star Formation Rates from Infrared and Radio Luminosities: The Origin of the Radio-Infrared Correlation. The Astrophysical Journal 586, 794–813. doi:10.1086/367829

[Matthews et al.(2021)] Matthews, A. M., Condon, J. J., Cotton, W. D., Mauch, T. 2021. Cosmic Star Formation History Measured at 1.4 GHz. The Astrophysical Journal 914. doi:10.3847/1538-4357/abfaf6

[Murphy et al.(2012)] Murphy, E. J. and 9 colleagues 2012. The Star Formation in Radio Survey: GBT 33 GHz Observations of Nearby Galaxy Nuclei and Extranuclear Star-forming Regions. The Astrophysical Journal 761. doi:10.1088/0004-637X/761/2/97

[Murphy(2013)] Murphy, E. J. 2013. The Role of Merger Stage on Galaxy Radio Spectra in Local Infrared-bright Starburst Galaxies. The Astrophysical Journal 777. doi:10.1088/0004-637X/777/1/58

[Howell et al.(2010)] Howell, J. H. and 23 colleagues 2010. The Great Observatories All-sky LIRG Survey: Comparison of Ultraviolet and Far-infrared Properties. The Astrophysical Journal 715, 572–588. doi:10.1088/0004-637X/715/1/572

# 8 Appendix

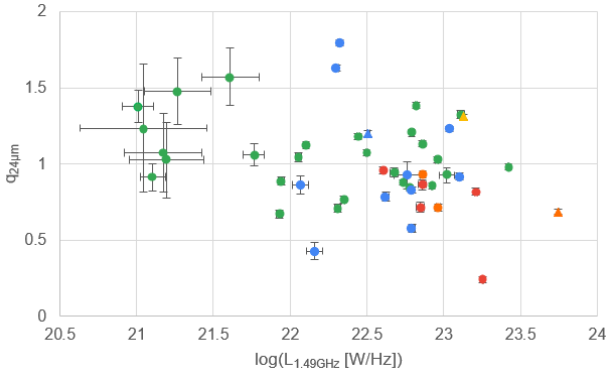


Figure 8: Plot of $q_{24}$ for resolved regions.

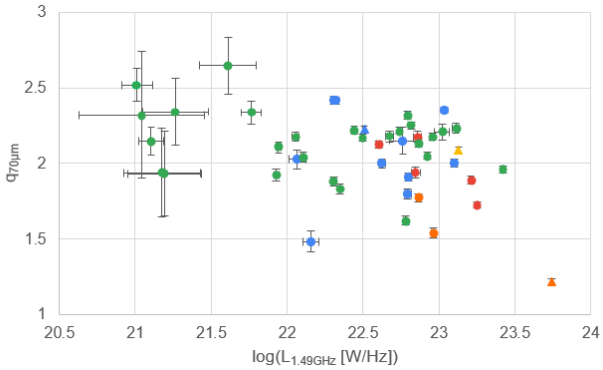


Figure 9: Plot of $q_{70}$ for resolved regions.

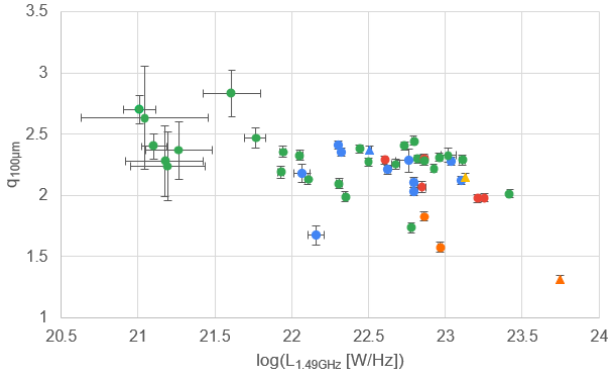


Figure 10: Plot of $q_{100}$ for resolved regions.

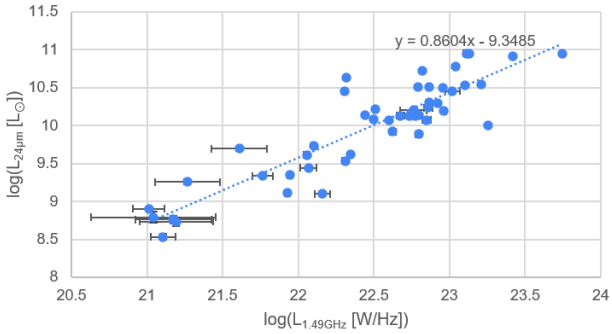


Figure 11: $\gamma_{24} = 0.860(64)$ for the full sample.

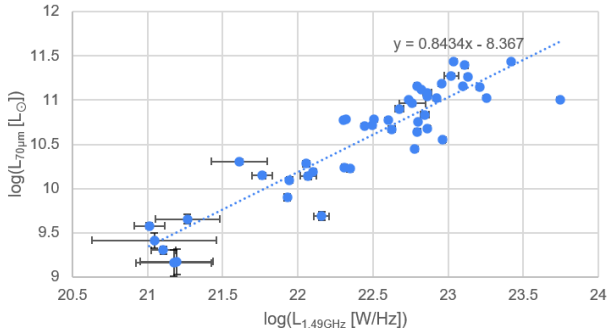


Figure 12: $\gamma_{70} = 0.843(56)$ for the full sample.

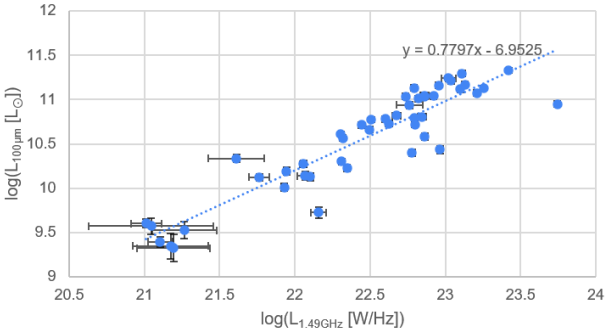


Figure 13: $\gamma_{100} = 0.780(51)$ for the full sample.